Adaptive Multiscale Sparse Unmixing for Hyperspectral Remote Sensing Image*

Yalan Li[1,2], Qian Du[3*], Yixuan Li[4], Wenwu Xie[4,*], Jing Yuan[5], Shang Lin Li[1,2,*],

and Qi Chen[6]

[1] Xiangnan University, Chenzhou,China
{liyalan, lsl}@xnu.edu.cn
[2] Hunan Engineering Research Center of Advanced Embedded Computing and Intelligent
Medical Systems, 423099 Chenzhou, China
{liyalan, lsl}@xnu.edu.cn
[3] Linyi University, Linyi, China
duqian@lyu.edu.cn
[4] Hunan Institute of Science and Technology, Yueyang, China
{812011120131-vip, gavinxie}@hnist.edu.cn
[5] Institute of Disaster Prevention, Beijing, China
yuanjing20110824@sina.com
[6] Hubei Normal University, Huangshi, China.
chenqi@hbnu.edu.cn

Abstract. Sparse unmixing of hyperspectral images aims to separate the endmembers and estimate the abundances of mixed pixels. This approach is the essential step for many applications involving hyperspectral images. The multi-scale spatial sparse hyperspectral unmixing algorithm (MUA) could achieve higher accuracy than many state-of-the-art algorithms. The regularization parameters, whose combinations markedly influence the unmixing accuracy, are determined by manually searching in the broad parameter space, leading to time consuming. To settle this issue, the adaptive multi-scale spatial sparse hyperspectral unmixing algorithm (AMUA) is proposed. Firstly, the MUA model is converted into a new version by using of a maximum a posteriori (MAP) system. Secondly, the theories indicating that andnorms are equivalent to Laplacian and multivariate Gaussian functions, respectively, are applied to explore the strong connections among the regularization parameters, estimated abundances and estimated noise variances. Finally, the connections are applied to update the regularization parameters adaptively in the optimization process of unmixing. Experimental results on both simulated data and real hyperspectral images show that the AMUA can substantially improve the unmixing efficiency at the cost of negligible accuracy. And a series of sensitive experiments were undertook to verify the robustness of the AMUA algorithm.

Keywords: adaptive multiscale sparse hyperspectral unmixing algorithm, loss functions, regularization parameters, *maximum a posteriori*.

---

* Corresponding authors

1.   Introduction

Hyperspectral remote sensing image (HRSI) is the data obtained by hyperspectral resolution sensors, which has led to extensive exploration in geology, medicine, aerial surveillance and other fields[1-7]. Numerous mixed pixels exist due to the low spatial resolution of the HRSI, which hinders the application of hyperspectral data. One of the key issues of HRSI systems lies in the separation of endmembers and the corresponding abundances from the mixed pixel[8-9]. This process is recognized as hyperspectral unmixing, which relies on a basic assumption of Linear Mixed Model (LMM); that is, the spectrum of a specific pixel is a linear mixture of the endmembers[8,10,11]. Sparse unmixing has attracted extensive recognition in the past few years with the increasing availability of spectral libraries. Sparse unmixing aims to estimate an abundance when the HRSI and spectral library are given in [12-19]. Thus, sparse unmixing usually is usually regarded as an ill-posed inverse problem, which indicates the absence of any unique solution. To alleviate such problems, a popular technique is widely used by adding regularizations to the loss function. Iordache et al.[20] considered that a pixel contains only a few numbers of components and introduce sparsity through the abundance map. In [20], the regularization was added to the abundance matrix to develop the sparse unmixing algorithm via variable splitting and augmented Lagrangian (SUnSAL). The SUnSAL has improved unmixing performance whilst ignoring the rich spatial correlation information among neighbouring pixels. For exploring spatial prior information, several sparse unmixing algorithms with the spatial prior information, such as SUnSAL with total variation (SUnSAL-TV) [21], have been introduced. The SUnSAL-TV utilized total variation regularization to estimate an abundance map, which has piecewise transitions at the cost of smoothing sharp discontinuities between neighbouring pixels. A new spectral﹣spatial weighted sparse unmixing (S2WSU) was developed to capture considerably sharp discontinuities[22]. S2WSU employed the spectral and spatial regularizations simultaneously to derive a sparse solution and obtain better abundance results[22]. However, this approach requires a considerable amount of time and is sensitive to noise. To overcome the limitations, Borsoi et al.[23] made use of multi-scale spatial information to develop a novel multi-scale sparse unmixing algorithm (MUA). In MUA, the original HRSI(in the original image domain) was transformed to a coarse-scale (CS) representation via means of segmentation techniques[24-28]. At this scale, the SUnSAL was used to estimate an initial abundance value. The initial abundance was then converted back to the original image domain to yield a low-level image, which is regarded as a novel information of the spatial context. A SUnSAL loss function was constructed in the original image domain. The new regularization term for the low-level image was added to this SUnSAL model to construct a novel unmixing mathematical model for the original HRSI. Therefore, MUA is the linear regression problem involving three regularization parameters. In the process of deducing the solutions, several existing works have reported that the estimated accuracy relies heavily on a proper configuration of these regularization parameters [29-34]. Given the desirable values, the MUA has achieved remarkable success in obtaining piecewise homogeneous abundances and sharp discontinuities among neighbouring pixels [23]. Unfortunately, the optimal regularization parameters in MUA are obtained by exhaustive search, which is unsuitable for real applications.

   A new format based on the MAP estimation technique is proposed for the solution of the regularization parameter selection problem for MUA. The MAP mainly aims to

identify the unknown fractional abundances including the regularization parameters by using the Bayes rule. As an effective adaptive parameter estimation method, the MAP system is used widely used for adaptively selecting regularization parameters in deep learning networks and image super-resolution [35-40]. To build the adaptive version of MUA, the MAP is applied to redesign the unmixing problem into a unified model to obtain the relations between the optimal regularization parameters and the fractional abundances.

Inspired by the idea in [35-37], an adaptive regularization parameters strategy for MUA is introduced, which is shown in Fig. 1.
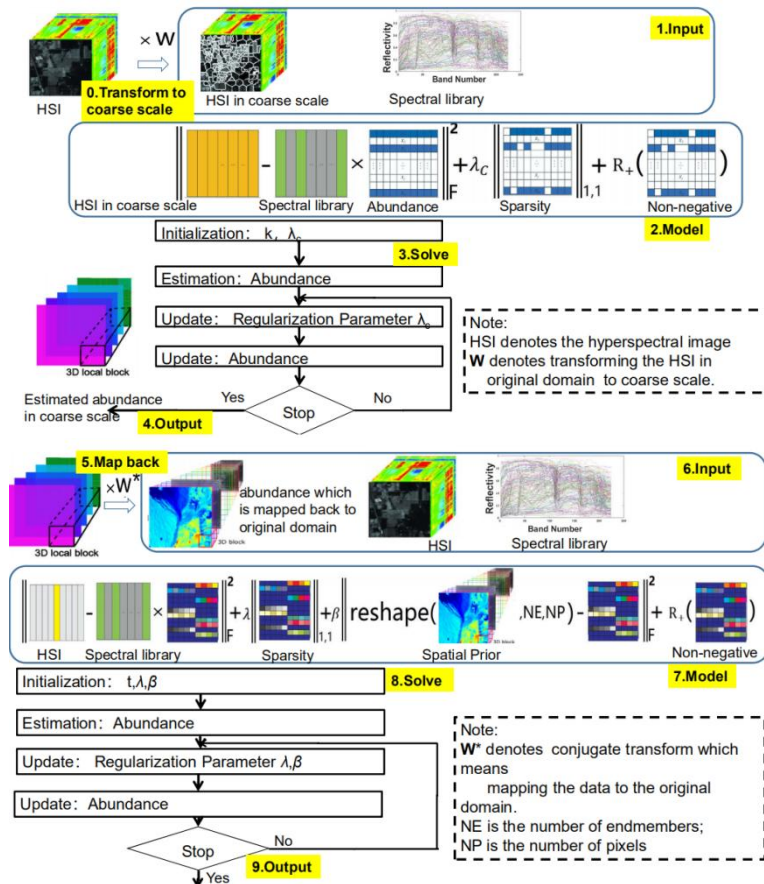

Fig.1. Framework of our proposed adaptive mutliscale spatial sparse unmixing scheme.

There are total 10 steps. At step 0, the HSI image is transformed to the coarse scale by W; At step 1, the HSI is inputted into the coarse scale and spectral libraries; At step 2, the model for unmixing the HSI in the coarse scale is constructed; At step 3, the model with adaptive regularization parameters scheme is solved; At step 4, the solution in coarse scale is obtained; At step 5, the solution by step 4 is mapped into the original domain; At step 6, the solution by step 4 is inputted to HSI and spectral libraries; At step 7, the model for unmixing with spatial prior is constructed; At step 8, the model by

step 7 with adaptive regularization parameters scheme is solved; At step 9, the final estimated abundance by automatic version of the multiscale spatial sparse unmixing algorithm is obtained. The major contributions are as follows.

1. The adaptive multi-scale spatial sparse unmixing strategy for MUA (AMUA) can adaptively choose the regularization parameters at each iteration in unmixing process.
2. The adaptive multi-scale spatial sparse unmixing strategy for MUA (AMUA) can adaptively choose the regularization parameters at each iteration in unmixing process.
3. The adaptive multi-scale spatial sparse unmixing strategy for MUA (AMUA) can adaptively choose the regularization parameters at each iteration in unmixing process.

The whole work is arranged as follows. The part 2 reviews the MUA method. The part 3 introduces the development process of the AMUA method in detail. The part 4 introduces numerous experiments and detailed comparisons. The part 5 discusses the sensitivity of the proposed method. Finally, the part 6 is the conclusion of the work.

2.   Review of Multi-scale Spatial Hyperspectral Unmixing

The section describes the framework of the multiscale sparse unmixing algorithm (MUA), which is closely related to the proposed method.

Let $Y \in \mathbb{R}^{L \times N}$ have L bands and N pixels, which is HRSI. The mixing process is modelled by the linear mixing model (LMM) [8], which is given as follows:

$$\mathbf{Y} = \mathbf{AX} + \mathbf{E}   \text{s.t.} : \mathbf{X} \geq \mathbf{0}, 1_P^T \mathbf{X} = 1_N^T , \tag{1}$$

where $\mathbf{A} = [\mathbf{a}_1, \mathbf{a}_2, \dots, \mathbf{a}_P] \in \mathbb{R}^{L \times P}$ represents an endmember spectral library with P endmembers; $\mathbf{X}$ is an abundance matrix and $\mathbf{X} = [\mathbf{x}_1, \mathbf{x}_2, \dots, \mathbf{x}_N] \in \mathbb{R}^{P \times N}$. $\mathbf{X} \geq \mathbf{0}$ and $1_P^T \mathbf{X} = 1_N^T$ is the abundance constraints (ANCs)[8]. Notation $[\cdot]^T$ represents vector/matrix transpose, and $\mathbf{E} \in \mathbb{R}^{L \times N}$ denotes an additive noise.

Only a few endmembers from library $\mathbf{A}$ are present in a pixel. Thus matrix $\mathbf{X}$ exhibits sparse property, and sparse unmixing can be specified as a function

$$\widehat{\mathbf{X}} = \text{argmin}_{\mathbf{X}} \frac{1}{2} ||\mathbf{Y} - \mathbf{AX}||_F^2 + \lambda ||\mathbf{X}||_{1,1} + R_+(\mathbf{X}) , \tag{2}$$

where $||\mathbf{X}||_{1,1}$ is the sparse regularization term and $R_+(\mathbf{X})$ represents non-negativity.

Therefore, the optimization problem of the MUA model can be written as follows [23]:

$$\widehat{\mathbf{X}_C} = \text{argmin}_{\mathbf{X}_C} \frac{1}{2} ||\mathbf{Y}_C - \mathbf{AX}_C||_F^2 + \lambda_C ||\mathbf{X}_C||_{1,1} , \tag{3}$$

$$\widehat{\mathbf{X}} = \underset{\mathbf{X} > 0}{\text{argmin}} ||\mathbf{Y} - \mathbf{AX}||_F^2 + \lambda ||\mathbf{X}||_{1,1} + \frac{\beta}{2} ||\widehat{\mathbf{X}_D} - \mathbf{X}||_F^2 , \tag{4}$$

where $\mathbf{W} \in \mathbb{R}^{N \times K}$ represents a transformation; $\mathbf{W}^* \in \mathbb{R}^{K \times N}$ denotes conjugate transform; $\mathbf{Y}_C = \mathbf{YW}$ represents the transformation of the original image $\mathbf{Y}$ to coarse approximations. $\mathbf{X}_C = \mathbf{XW}$ means transforming the abundance matrix $\mathbf{X}$ to the corresponding coarse scale. $\widehat{\mathbf{X}_C}$ is the abundance estimated by equation (3) in coarse

scale and $\widehat{\mathbf{X}_D} = \widehat{\mathbf{X}_C}\mathbf{W}^*$ stands for mapping the $\widehat{\mathbf{X}_C}$ back to the original image domain to yield the coarse abundance $\widehat{\mathbf{X}_D}$. Lastly, $\widehat{\mathbf{X}}$ is the final solution to MUA [23]. λ, β and λc are the regularisation parameters.

3.   Adaptive Multi-scale Spatial Sparse Hyperspectral Unmixing

This section describes the use of MAP to investigate the relationships among the estimated abundance, regularization parameters and the noise variance of the HRSI. These relationships are applied to the alternating direction multiplier (ADMM) algorithm [41] to settle the problem of adaptive multiscale spatial sparse unmixing.

The multi-scale spatial sparse unmixing comprises two mathematical models in (3) and (4). Firstly, the model in (4) is investigated: given $\mathbf{Y}$ and $\mathbf{A}$, $\mathbf{X}$ is estimated together with the parameters λ and β. Under the Bayesian framework and MAP, the unmixing model in (4) can be reconsidered as estimating the λ, β and $\mathbf{X}$ at the same level and the problem can be rewritten as:

$$(\widehat{\mathbf{X}},\lambda,\beta) = \underset{\mathbf{X}>0}{\mathrm{argmax}}(p(\mathbf{X},\lambda,\beta|\mathbf{Y})) . \tag{5}$$

Using Bayes' rule, (5) can be expressed as:

$$(\widehat{\mathbf{X}},\lambda,\beta) = \underset{(\mathbf{X},\lambda,\beta)}{\mathrm{argmax}}(\frac{p(\mathbf{Y}|\mathbf{X},\lambda,\beta)p(\mathbf{X}|\lambda,\beta)p(\lambda,\beta)}{p(\mathbf{Y})}) . \tag{6}$$

The λ, β and $\mathbf{X}$ are independent of $p(\mathbf{Y})$; thus (6) is equivalent to (7):

$$(\widehat{\mathbf{X}},\lambda,\beta) = \underset{(\mathbf{X},\lambda,\beta)}{\mathrm{argmax}}(p(\mathbf{Y}|\mathbf{X},\lambda,\beta)p(\mathbf{X}|\lambda,\beta)p(\lambda,\beta) , \tag{7}$$

where $(p(\mathbf{Y}|\mathbf{X},\lambda,\beta)$ is the likelihood distribution of the $\mathbf{X}$ equal to $p(\mathbf{Y}|\mathbf{X})$. Suppose $\mathbf{Y}$ is polluted by zero-mean white Gaussian noise, the probability distribution of $p(\mathbf{Y}|\mathbf{X})$ is as follows:

$$P(\mathbf{Y}|\mathbf{X}) = \frac{1}{\sqrt{2\pi}\delta_n}\exp\left(-\frac{||\mathbf{Y}-\mathbf{A}\mathbf{X}||_F^2}{2\delta_n^2}\right) , \tag{8}$$

where δ_n is the standard deviation of the Gaussian noise.

For the abundance matrix $\mathbf{X}$ with sparse property and spatial prior information, Borsoi et al. indicated that $||\mathbf{X}||_{1,1}$ corresponds to a Laplacian probability with zero-mean [22]. Wang et al. reported that $||\widehat{\mathbf{X}_D} - \mathbf{X}||_F^2$ can be regarded as an independent and identically distributed multivariate Gaussian prior with a zero-mean value [12,42]. Therefore, the prior density $P(\mathbf{X})$ could be written as

$$P(\mathbf{X}) = \frac{1}{C}\exp\left(-\frac{\sqrt{2}||\mathbf{X}||_{1,1}}{\delta_x}\right) \cdot \exp\left(-\frac{||\widehat{\mathbf{X}_D} - \mathbf{X}||_F^2}{2\delta_\beta^2}\right)$$

$$= \frac{1}{c}\exp\left(-\frac{\sqrt{2}||\mathbf{X}||_{1,1}}{\delta_x} - \frac{||\widehat{\mathbf{X}_D}-\mathbf{X}||_F^2}{2\delta_\beta^2}\right) , \tag{9}$$

where C is the normalization factor related to the sum of the succeeding exponential function and δ_β stands for the standard deviation of the map acquired by the $\widehat{\mathbf{X}_D} - \mathbf{X}$. δ_x is the standard deviation of the abundance X.

The prior for $p(\lambda, \beta)$ is a uniform distribution [37]. Substituting (8) and (9) in (7) yields

$$(\widehat{X}, \lambda, \beta) = \underset{(X,\lambda,\beta)}{\mathrm{argmax}}(log \mathrm{p}(Y|X, \lambda, \beta) + log \mathrm{p}(X|\lambda, \beta) + log \mathrm{p}(\lambda, \beta))$$

$$= \underset{(X,\lambda,\beta)}{\mathrm{argmax}}(-\frac{||Y-AX||_F^2}{2\delta_n^2} - \frac{\sqrt{2}||X||_{1,1}}{\delta_x} - \frac{||\widehat{X_D}-X||_F^2}{2\delta_\beta^2} + log \mathrm{p}(\lambda, \beta) + log C1 + log C2)$$

$$= \underset{(X,\lambda,\beta)}{\mathrm{argmin}}(\frac{||Y-AX||_F^2}{2\delta_n^2} + \frac{\sqrt{2}||X||_{1,1}}{\delta_x} + \frac{||\widehat{X_D}-X||_F^2}{2\delta_\beta^2}), \tag{10}$$

where $log C1$ is the irrelevant term from $\mathrm{p}(X|\lambda, \beta)$ and $\mathrm{p}(Y|X, \lambda, \beta)$. C2 is the standardized constant related to the stable prior value of $p(\lambda, \beta)$.

From (4) and (10), the relationships between the regularization parameters λ, β and the unknown abundance X can be determined by the following:

$$\lambda = \frac{\sqrt{2}\delta_n^2}{\delta_x}, \beta = \frac{\delta_n^2}{\delta_\beta^2}. \tag{11}$$

Similarly, the above processing is performed on (3) to obtain the following:

$$\lambda_C = \sqrt{2}\delta_{Y_C}^2/\delta_{X_C}. \tag{12}$$

where δ_{X_C} and δ_{Y_C} are the standard deviations of the abundance X_C and image Y_C, respectively.

Table 1. Algorithm 1: AMUA

Algorithm 1: AMUA
1. **Input:** $A; Y_C$; set $k = 1$; $X_c^{(0)} = (A^TA + 3I)^{-1}(A^TY_C)$; Max_Iter=50; choose $\lambda_c^{(0)} > 0$ randomly. **Repeat** $X_c^{(k)} = \mathrm{argmin}_{X_C}\frac{1}{2}||Y_C - AX_C||_F^2 + \lambda_c^{(k-1)}||X_C||_{1,1}$; $\delta_{Y_C}^{(k)} = \mathrm{std}(Y_C - AX_c^{(k)}))$; $\delta_{X_C}^{(k)} = \mathrm{std}(X_c^{(k)})$; $\lambda_c^{(k)} = \frac{\sqrt{2}(\delta_{Y_C}^{(k)})^2}{\delta_{X_C}^{(k)}}$; **Until:** $\mathrm{abs}(\lambda_c^{(k)} - \lambda_c^{(k-1)}) \leq 1e-6$ or $k \geq$ Max_Iter **Output:** $\widehat{X_C} = X_c^{(k)}$ 2. Input: $A; Y; \widehat{X_D} = \widehat{X_C}W^*$; set $t = 1$; Max_Iter = 50; choose $\lambda^0, \beta^0 > 0$ randomly; **Repeat:** $\widehat{X}^{(t)} = \underset{X>0}{\mathrm{argmin}}\frac{1}{2}||Y - AX||_F^2 + \lambda^{(t-1)}||X||_{1,1}$ $\qquad + \frac{\beta^{(t-1)}}{2}\left\|\widehat{X_D} - X\right\|_F^2$ $\delta_n^{(t)} = \mathrm{std}(Y - A\widehat{X}^{(t)})$; $\delta_X^{(t)} = \mathrm{std}(\widehat{X}^{(t)})$ $\lambda^{(t)} = \frac{\sqrt{2}(\delta_n^{(t)})^2}{\delta_x^{(t)}}$; $\delta_\beta^{(t)} = \mathrm{std}(\widehat{X}^{(t)} - \widehat{X_D})$; $\beta^{(t)} = \frac{(\delta_n^{(t)})^2}{\delta_\beta^{(t)}}$; **Until:** $\mathrm{abs}(\lambda^{(t)} - \lambda^{(t-1)}) \leq 1e-6$; and; $\qquad \mathrm{abs}(\beta^{(t)} - \beta^{(t-1)}) \leq 1e-6$; or $t \geq$ MaxIter **Output:** $\widehat{X} = \widehat{X}(t)$

Lastly, (13) lists the summary of regularization parameters.

$$
\left.
\begin{array}{l}
\lambda = \frac{\sqrt{2}\delta_n^2}{\delta_x} \\[2mm]
\beta = \frac{\delta_n^2}{\delta_\beta^2} \\[2mm]
\lambda_C = \frac{\sqrt{2}\delta_{Y_C}^2}{\delta_{x_C}}
\end{array}
\right\}.
\tag{13}
$$

Observing (13), strong relationships are found between the regularization parameters and the standard deviations (δ_n, δ_x, δ_β, δ_{Y_C}, δ_{x_C}). These standard deviations are unknown in the real HRS and are usually estimated as follows: δ_n is estimated by the method in [43], δ_x and δ_{x_C} result from the abundance estimated at the corresponding iteration. The details will be described in the Algorithm 1.

The main iterative process of AMUA is listed in Algorithm 1 using the (ADMM) strategy [41], which can degrade the complex problem into a series of simple ones and efficiently solve AMUA. Notably, the transformation $\mathbf{W}$, which was mentioned after Equation (4), appears in Algorithm 1. The $\mathbf{W}$ denotes the operation of transforming the original image to a coarser scale [23], such as a segmentation with binary partition tree (BPT) [44] and over-segmentation with the simple linear iterative clustering (SLIC)[45]. Additional details will be presented in section 4.

4.   Experiments

In this part, numerous experiments were performed on two simulated datasets (DC1 and DC2), and one real HRSI to illustrate the accuracy and effectiveness of the proposed algorithms. The proposed method AMUA has two alternatives: AMUA using BPT segmentation (denoted as AMUA (BPT)) and that using SLIC segmentation (denoted as AMUA (SLIC)). The proposed methods are compared with MUA using BPT (denoted as MUA(BPT)) [23], MUA using SLIC (MUA(SLIC)) [23], SUnSAL [20], SUnSAL-TV [21] and S2WSU [22].

The optimal regularization parameters(λ, β, λ_C) are manually selected by performing a grid search for different datasets in SUnSAL, SUnSAL-TV, S2WSU and MUA algorithms. For the different datasets, Table 2 lists the optimal parameters given in [20], [21], [22], [23]. Notably, the regularization parameters(λ, β, λ_C) in AMUA algorithms are automatically estimated by an alternating iterative process. Hence, the parameters in AMUA algorithm are not constant and denoted by NA in Table 2.

Table 2. Parameters

Algorithms / Data	DC1 data cube		DC2 data cube		Curprit
	20dB	30dB	20dB	30dB	
SUnSAL	$\lambda = 0.7$	$\lambda = 0.1$	$\lambda = 0.1$	$\lambda = 0.01$	$\lambda = 0.01$
SUnSAL-TV	$\lambda = 0.05$	$\lambda = 0.007$	$\lambda = 0.01$	$\lambda = 0.005$	$\lambda = 0.001$
	$\lambda_{TV} = 0.05$	$\lambda_{TV} = 0.01$	$\lambda_{TV} = 0.03$	$\lambda_{TV} = 0.007$	$\lambda_{TV} = 0.001$
S2WSU	$\lambda = 0.1$	$\lambda = 0.005$	$\lambda = 0.01$	$\lambda = 0.01$	$\lambda = 7E(-5)$
MUA(BPT)	$\lambda = 0.1$	$\lambda = 0.1$	$\lambda = 0.1$	$\lambda = 0.05$	$\lambda = 0.001$
	$\lambda_C = 0.005$	$\lambda_C = 0.005$	$\lambda_C = 0.005$	$\lambda_C = 0.001$	$\lambda_C = 0.001$
	$\beta = 30$	$\beta = 30$	$\beta = 5$	$\beta = 1$	$\beta = 3$
AMUA(BPT)	**NA**	**NA**	**NA**	**NA**	**NA**
MUA(SLIC)	$\lambda = 0.1$	$\lambda = 0.05$	$\lambda = 0.1$	$\lambda = 0.03$	$\lambda = 0.001$
	$\lambda C = 0.03$	$\lambda C = 0.007$	$\lambda C = 0.007$	$\lambda C = 0.003$	$\lambda C = 0.001$
	$\beta = 30$	$\beta = 10$	$\beta = 10$	$\beta = 3$	$\beta = 30$
AMUA(SLIC)	**NA**	**NA**	**NA**	**NA**	**NA**

4.1.   Simulated and real datasets for efficiency comparison

To illustrate the efficiency, Table 3 lists the running times of SUnSAL, SUnSAL-TV, S2WSU, MUA and AMUA for DC1, DC2 and Cuprite data. All the algorithms were carried out on PC, using MATLAB R2019b, an Intel Core i5-8250u CPU (1.6 GHz) and 8.00 GB RAM. For SUnSAL, SUnSAL-TV, S2WSU and MUA, the regularization parameters (λ, β, λ_C) are computed by a loop running many times with different combinations of some parameters until the best unmixing result is obtained. In most cases, the total number combinations of the parameters (TNCP) amounts to 100 at least. And for one combination, the executing time (ET) is different for different algorithms. Hence, the running time is computed by multiplying TNCP with ET. Since the parameters are estimated automatically in AMUA, there are not many parameter combinations, so the TNCP is equal to one. Compared with all other algorithms in Table 3, the AMUA efficiency is greatly improved and the total running time is greatly reduced. For DC2 instance, the total running times for SUnSAL, SUnSAL-TV, S2WSU, MUA(BPT), MUA(SLIC), AMUA(BPT) and AMUA(SLIC) are 1046.3s, 17108s, 9130.5s, 1121.7s, 650.6s, 160.496s and 74.021s. The greatly improved efficiency mainly result from that the AMUA avoids extensive search for optimal parameters.

Table 3. Running times (Simulated database for accuracy comparison)

Data Algorithms	SUnSAL	SUnSAL-TV	S2WSU	MUA (BPT)	MUA (SLIC)	AMUA (BPT)	AMUA (SLIC)
DC1	5.187s×100	164.839s×100	50.063s×100	14.947s×100	7.164s×100	23.028s×1	19.869s×1
DC2	10.463s×100	171.08s×100	91.305s×100	11.217s×100	6.506s×100	160.496s×1	74.021s×1
Real mage	368.7s×100	2290.4s×100	961.8s×100	157.9s×100	202.5s×100	1107.8ss×1	997.34s×1

4.2.   Simulated database for accuarcy comparison

Data cube DC1, which comprises 5 endmembers, has 75×75 pixels[20]. Meanwhile, data cube DC2 containing piecewise smooth abundance maps (with steep transitions) has 9 endmembers and 100×100 pixels[23]. In DC1 and DC2, the observed HRSIs were contaminated by white Gaussian noise, with signal-to-noise ratios (SNR) of 20 and 30dB[23]. To assess the accuracy of unmixing, the signal-to-reconstruction error (SRE)[21] is defined as shown below:

$$\mathrm{SRE} = 10\log_{10}\mathbb{E}\{||\mathbf{X}||_{\mathrm{F}}^2\} / \mathbb{E}\{||\hat{\mathbf{X}} - \mathbf{X}||_{\mathrm{F}}^2\} ,   (13)$$

where $\mathbf{X}$ and $\hat{\mathbf{X}}$ are the true and estimated abundance, respectively; a high SRE value for the estimated abundance leads to high estimated accuracy.

Table 4 lists the SRE values of different algorithms for the data DC1 and DC2. And Fig.2 shows these values directly in a histogram. Compared with MUA, the SRE value of AMUA is slightly lower, near to that of MUA. For DC1 with a 20 dB instance, the SRE value of AMUA (BPT) achieves 12.715, the SRE of MUA(BPT) is 13.393, and the difference is only approximately 0.68. Meanwhile, the results of the AMUA algorithm were significantly better than those of SUnSAL(4.541), SUnSAL-TV(9.424) and S2WSU(7.697).

Table 4. SRE values of different algorithms on DCI and DC2.

Algorithms / Data	DC1 data cube		DC2 data cube	
	20dB	30dB	20dB	30dB
SUnSAL	4.541	8.911	4.281	10.428
SUnSAL-TV	9.424	14.441	11.554	17.988
S2WSU	7.697	15.487	9.332	21.668
MUA(BPT)	13.393	**18.257**	**13.928**	16.963
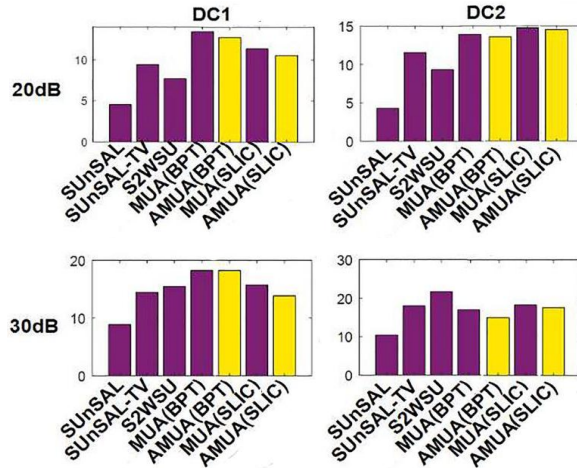
Fig. 2. SRE values of different algorithms on DC1 and DC2 by histogram

Compared with S2WSU, the SRE values of AMUA are more stable. The SRE values of S2WSU for DC2 with 30 dB instance achieve the best performance (21.668) among

listed algorithms. However, the SRE value of S2WSU degrades rapidly to 9.332 when the SNR is decreased to 20 dB. The SRE values of AMUA(BPT) for DC2 30 and 20 dB are 16.963 and 13.928, respectively. The SRE values of AMUA(SLIC) for DC2 30 and 20 dB are 17.60 and 14.488, respectively, demonstrating a stable performance.

Figs. 3 and 4 show abundance map samples from different algorithms for the second endmember of DC1 and DC2, respectively, with the upper row 20 DB SNR and the lower row 30 DB SNR.

Fig. 3 shows that the global differences between MUA and AMUA are too small to be observed, especially those between MUA(BPT) and AMUA(BPT), as shown in the red rectangles. Fig. 4 shows that compared with MUA, AMUA can improve the sharpness of edge regions between adjacent regions, such as green ellipse regions, and obtain more smooth homogeneous areas, such as the region in the yellow circle.
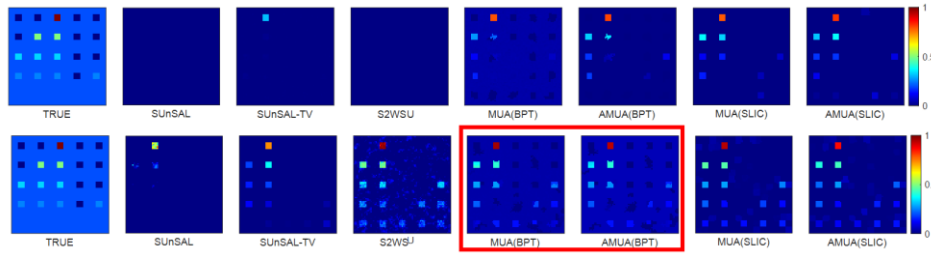

Fig. 3. Abundance maps obtained by different unmixing algorithms for the second endmember in DC1
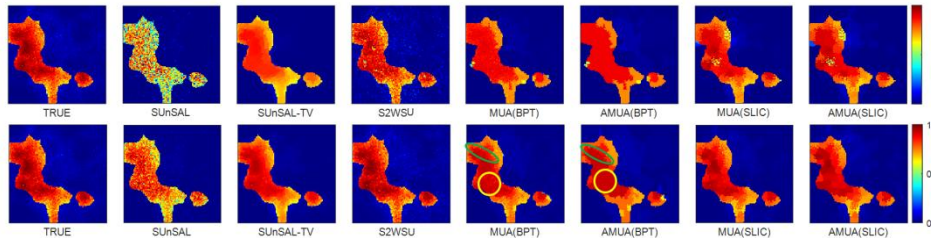

Fig. 4. Abundance maps obtained by different unmixing algorithms for the second endmember in DC2

4.3.   Real hyperspectral image for accuracy comparison

To evaluate the robustness of the proposed AMUA algorithm, qualitative comparisons were constructed using Cuprite, a well-known and widely used real data set provided in [43]. The abundance images estimated by different algorithms for the minerals alunite, buddingtonite and chalcedony are shown in Fig. 5, arranged from top to bottom. The AMUA algorithms can obtain similar abundance to that of MUA algorithms. However, some parts from AMUA (BPT) are smoother than that of MUA (BPT), such as the parts highlighted by the ellipses in Fig. 5. The edge parts by AMUA (BPT) are also sharper than by MUA (BPT), such as the areas highlighted by the rectangle in Fig. 5.
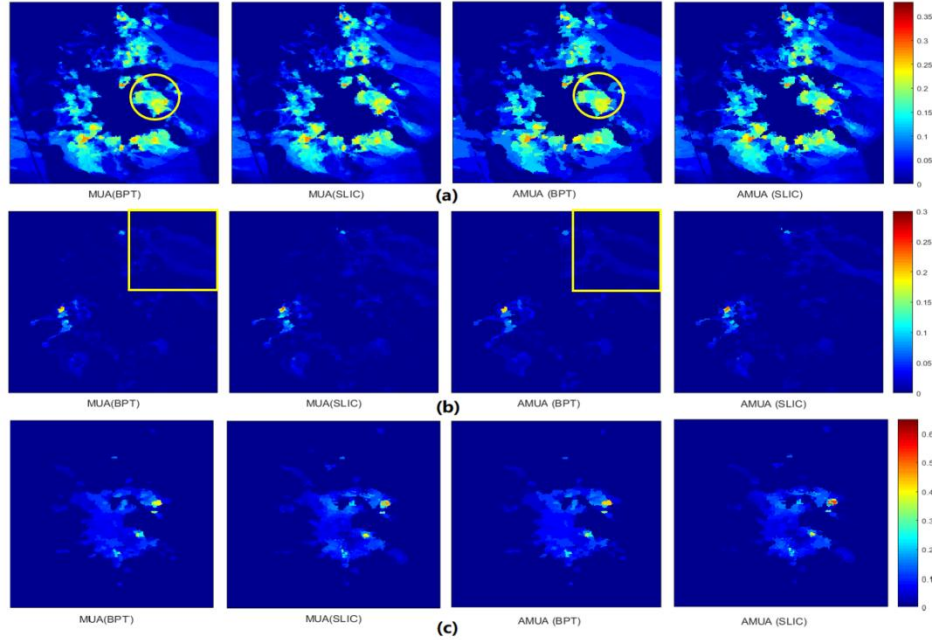
Fig. 5. Abundance maps of different algorithms methods for the data Cuprite.

5.   Sensitivity discussion

This section will analyse the sensitivity of the AMUA algorithm to the regularization parameters (λ, β, λ_C), the estimated noise and the estimated abundance.

5.1.   Sensitivity to regularization parameters

In the MUA, three regularization parameters(λ, β, λ_C) are manually selected to trade off the original image sparsity (λ), coarse scale sparsity (λ_C) and multiscale spatial information (β). The determination of the regularization parameters (λ,β,λ_C) greatly affects the unmixing performance. The regularization parameters(λ,β , λ_C) are automatically determined in AMUA.The impact of λ, β, and λ_C on the accuracy of unmixing results with DC1 20 and 30 dB by using MUA and AMUA algorithms are shown in Figs. 6 and 7, respectively. The 4-D colour-maps illustrate the SRE values (corresponding to the bubble colour) at different combinations of λ, β and λ_C. For example, in the Fig.7 (a), the bubble A exhibits shallow blue, which denotes the SRE as 12.321 at a combination of λ=0,β=1000 and λ_C=0. The values of the regularization parameters are searched within {0,1e-15,1e-13,1e-11,1e-9,1e-7,1e-5, 1e-3 ,1e-1, 1e0, 1e1 ,1e2 ,1e3}. The sub-figures (a) and (c) in Figs. 6 and 7 illustrate the searching details in the MUA (BPT) and MUA (SLIC) algorithms, respectively. The combinations of λ, β and λ_C are automatically determined in AMUA algorithms. And the sub-figures

(b) and (d) display the performance of the AMUA (BPT) and AMUA (SLIC) algorithms, respectively.

The following conclusions are presented on the basis of Figs. 6 and 7.

(1) For the MUA, satisfactory accuracy can be achieved by carefully selecting appropriate combinations of the regularization parameters. For example, in Fig.6 (a), the highest SRE value (approximately 12.627 dB) occurs at λ = 1e-3, β = 1 and λ_C =1e-1; however, poor accuracy, such as the SRE value(-6.50 dB), occurs at improper combinations of regularization parameters. The AMUA not only obtains the acceptable accuracy, but also avoids searching the regularization parameters manually.

(2) The optimal regularization parameters vary for different datasets; such a variation would be a burden for manually searching the regularization parameters in practice. For MUA (SLIC) under DC1 20 dB instance, the highest accuracy can be achieved at λ = 1e-3, β = 1e2 and λ_C=0.001. However, the highest accuracy under DC2 30 dB can be obtained in a different combination of λ = 1e-4, β = 1e-3 and λ_C = 1000.

(3) The AMUA algorithm could achieve relatively satisfactory results on test data sets by effectively determining regularization parameters adaptively. Figs. 6 and 7 demonstrate that the bubbles obtained by the AMUA share the same colour as the high accuracy bubbles obtained by MUA.
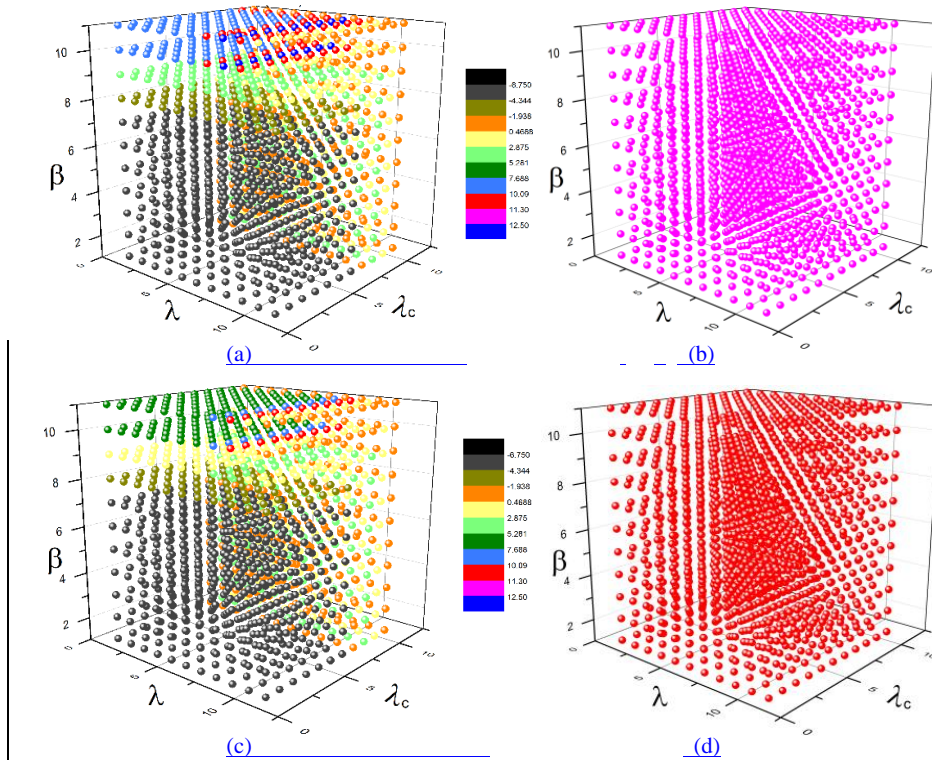

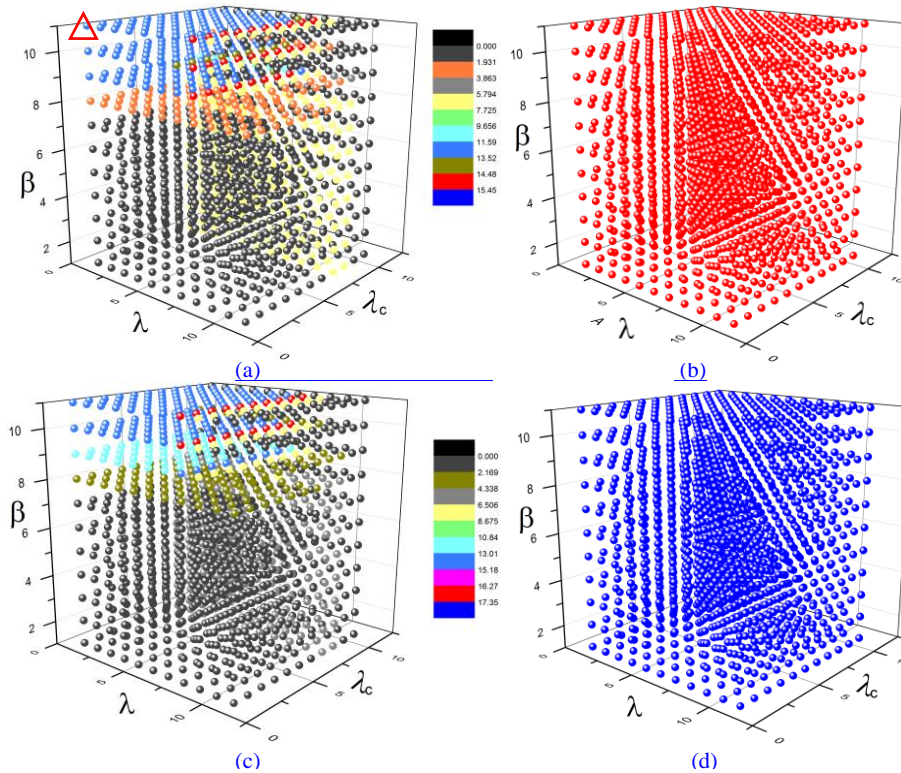**Fig. 6.** SRE in relation with regularization parameters λ, β and λ_C for DC1 20dB

5.2. Sensitivity to the noise variance estimated from the HRSI

The noise variance δ_n^2 estimated following the method proposed in reference [43] is a crucial parameter in the ADMM and affects the conduct of the unmixing algorithms. However, the estimated results are usually unstable. Experiments are performed on the data cube DC2 (20 dB), DC2 (30 dB), DC2(40 dB) and the Cuprite to understand the effects effectively. The fluctuation of noise (FR) is defined as follows:

$$FR = \frac{VNV - TNV}{TNV}, \tag{14}$$

where TNV represents the true noise variance of the HRSI. VNV denotes the estimated noise variance for the HRSI. FR represents the fluctuation degree, which ranges within [-1, -0.01, -0.05, -0.1, -0.5, 0, 0.01, 0.05, 0.1, 0.5, 1, 5, 10, 50, 100, 1000 and 10000]. Different VNV values could be obtained for sensitive experiments by using (15), providing the TNV and different FR values. Notably, FR = 0 means that the VNV is estimated accurately, which is equal to the truth value. Meanwhile, FR = -1 means the VNV = 0.

$$VNV = TNV + FR \times TNV. \tag{15}$$

Fig. 7. SRE in relation with regularization parameters λ, β and λ_C for DC2 30dB

In the AMUA, the different values of the VNV are utilized to obtain different values for $\delta_n^{(t)}$ to derive various unmixing results. The relationship curves between SRE and the FR are shown in Fig. 8. The horizontal and vertical axis denote FR and SRE , respectively. The turquoise and yellow marker denote the SRE obtained with the true noise variance. The red and blue markers denote the SRE obtained with fluctuating estimated noise variance. From the Fig. 8, the following conclusions can be drawn.

1.   In the absence of noise with FR = −1, which is impractical, the unmixing accuracy is low (i.e. the SRE falls to 1.667 in Fig. 8(b)).
2.   The small fluctuation of the estimated noise variance cannot affect the unmixing performance significantly, such as in Fig. 8(b). In this figure, the SRE(SLIC) at location (FR = 0.01) is 17.595, whilst that obtained with the true noise is 17.6, demonstrating a difference of 0.005.
3.   The unmixing accuracy decreases with the increase in the fluctuation of the VNV. For instance, in Fig. 8(a), the SRE(SLIC) at the location FR = 0 is 14.488, whilst that at FR = 1000 decreases to 14.327.

The ground truth for the Cuprite data is not provided. Thus, the true noise variance in HRSI is estimated by the method in [43], and the value(TNV) is 7.2659e-06, which is regarded as the truth noise variance. Different VNV values are employed in the AMUA to generate different abundance maps, as shown in Figs. 9,10 and 11. The abundance maps in each subfigure (f) are regarded as the ground truth maps. These maps reveal that the accuracy of AMAU is relatively insensitive to the fluctuation of the VNV. For example, in Fig. 9, most sub-figures are similar to the ground truth map, except for the maps in Figs. 9(a) and 9(h), which are far away with extreme FR values. The FR in Fig. 9 (a) is -1, which means that the noise variance VNV is 0, namely the HRSI is in the absence of noise. For FR in Fig. 9 (h) is 10000, which means that the fluctuation of the noise variance is extremely large.
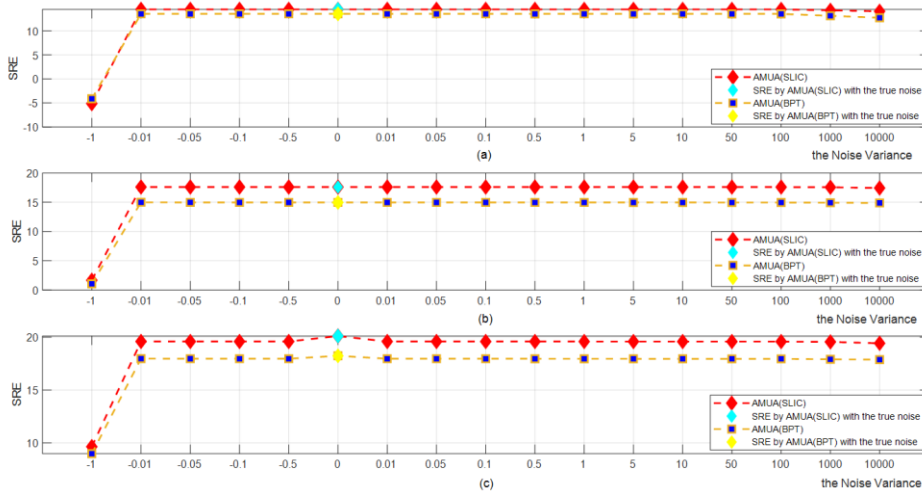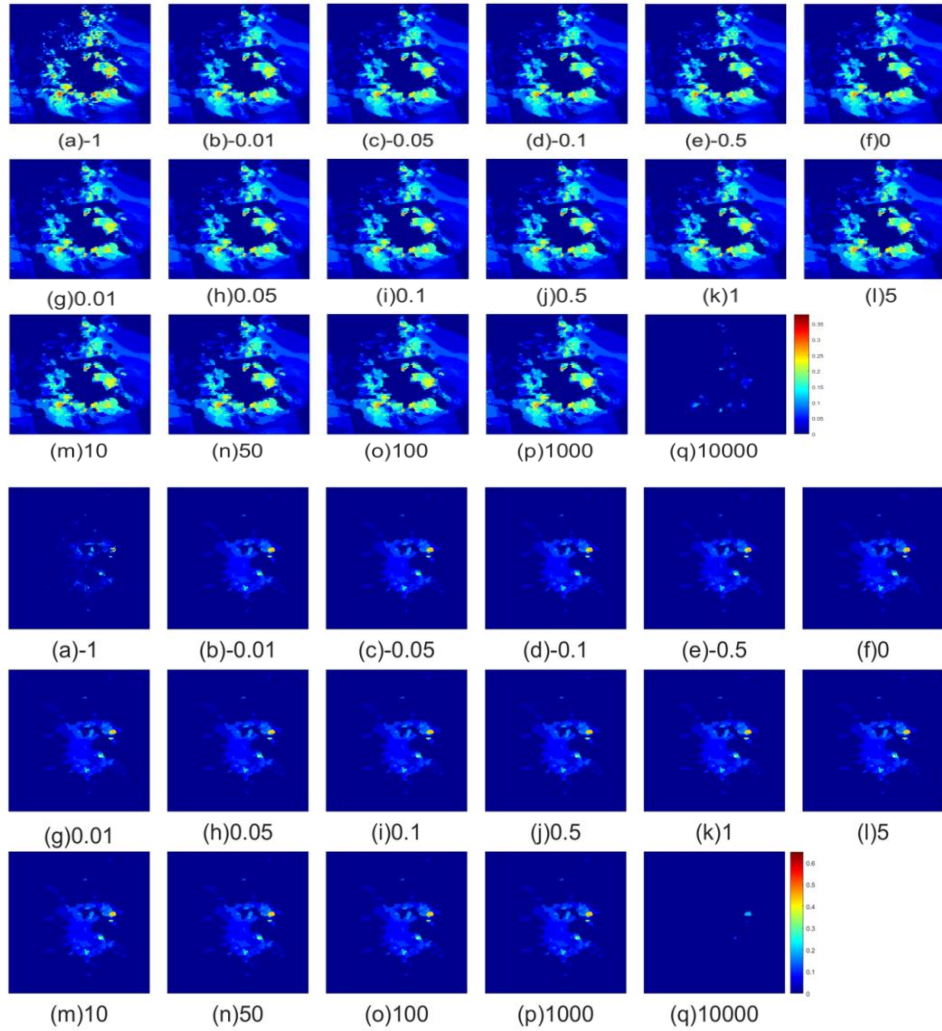

Fig. 8. SRE in relation to noise variance fluctuation for DC2.

The results generally illustrate the robustness of the AMUA to the small fluctuation of the VNV.

(a)-1   (b)-0.01   (c)-0.05   (d)-0.1   (e)-0.5   (f)0

(g)0.01   (h)0.05   (i)0.1   (j)0.5   (k)1   (l)5

(m)10   (n)50   (o)100   (p)1000   (q)10000

(a)-1   (b)-0.01   (c)-0.05   (d)-0.1   (e)-0.5   (f)0

(g)0.01   (h)0.05   (i)0.1   (j)0.5   (k)1   (l)5

(m)10   (n)50   (o)100   (p)1000   (q)10000

Fig. 10. The Buddingtonite abundance images considering the noise variance fluctuation
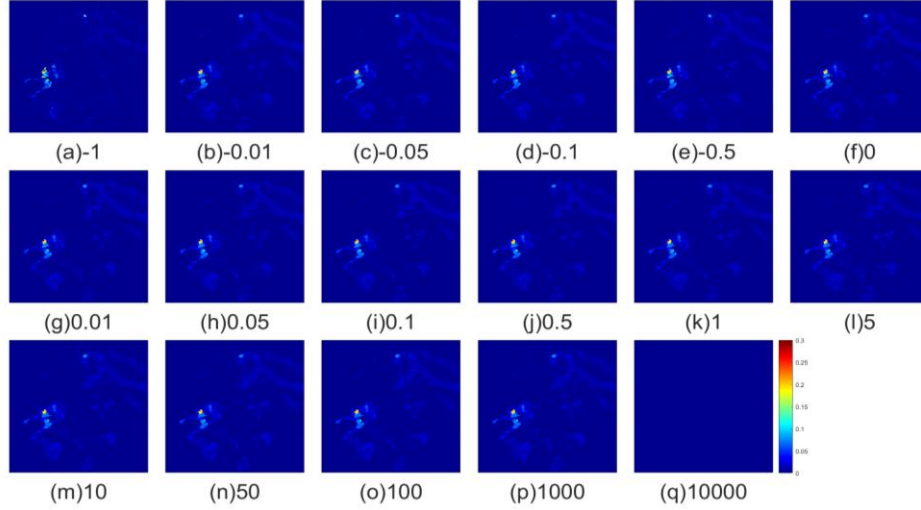
Fig. 11. The Chalcedony abundance images considering the noise variance fluctuation.

5.3.   Sensitivity to the variance of the abundance updated at each iteration.

The detailed process of updating the regularization parameters in AMUA is presented as follows:

$$\lambda^{(t)} = \sqrt{2}(\delta_n^{(t)})^2/\delta_X^{(t)}(\text{where } \delta_X^{(t)} = \text{std}(\widehat{\mathbf{X}}^{(t)})),$$
$$\lambda_c^{(k)} = \sqrt{2}(\delta_{Y_C}^{(k)})^2/\delta_{X_C}^{(k)}(\text{where } \delta_{X_C}^{(k)} = \text{std}(\mathbf{X}_c^{(k)})), \tag{16}$$
$$\beta^{(t)} = (\delta_n^{(t)})^2/\delta_\beta^{(t)}; (\text{where } \delta_\beta^{(t)} = \text{std}(\widehat{\mathbf{X}}^{(t)} - \widehat{\mathbf{X}_D})).$$

The regularization parameters are updated according to $\widehat{\mathbf{X}}^{(t)}$, which is the estimated abundance obtained at iteration t.

For comparison, in the process of solving AMUA, $\widehat{\mathbf{X}}^{(t)}$ is replaced with the true abundance **X** denoted as AMUA-GT. That is, the parameters are set as follows:

$$\lambda^{(t)} = \sqrt{2}(\delta_n^{(t)})^2/\delta_X^{(t)}(\text{where } \delta_X^{(t)} = \text{std}(\mathbf{X})),$$
$$\lambda_c^{(k)} = \sqrt{2}(\delta_{Y_C}^{(k)})^2/\delta_{X_C}^{(k)}(\text{where } \delta_{X_C}^{(k)} = \text{std}(\mathbf{X}_c^{(k)})),$$
$$\beta^{(t)} = (\delta_n^{(t)})^2/\delta_\beta^{(t)}; (\text{where } \delta_\beta^{(t)} = \text{std}(\mathbf{X} - \widehat{\mathbf{X}_D})). \tag{17}$$

The abundance images estimated by AMUA, AMUA-GT and other different algorithms are shown in Fig. 12 and Fig. 13 ,with subfigure (a) under 20 dB, subfigure (b) under 30 dB and subfigure (c) under 40 dB. The corresponding SRE values are also listed in Table 5.

From Fig. 12 and Fig. 13, It can be revealed that the difference between the abundances estimated by AMUA-GT and AMUA is insignificant. And the same conclusion can be drawn in Table 5. For DC1 with 30 dB instance, the SRE values of AMUA-GT (BPT) and AMUA(BPT) are 18.281 and 18.217, respectively. The difference is only 0.052. For DC1 with 40 dB instance, the SRE values of AMUA-GT

(BPT) and AMUA(BPT) are 21.959 and 21.806, respectively. The tiny difference is 0.153. For DC2 with 20 dB instance, the SRE values of AMUA-GT (SLIC) and AMUA (SLIC) are 14.77 and 14.488, respectively. The difference 0.286 is also very small. So the AMUA is insensitive to the variation of the abundance updated at each iteration.
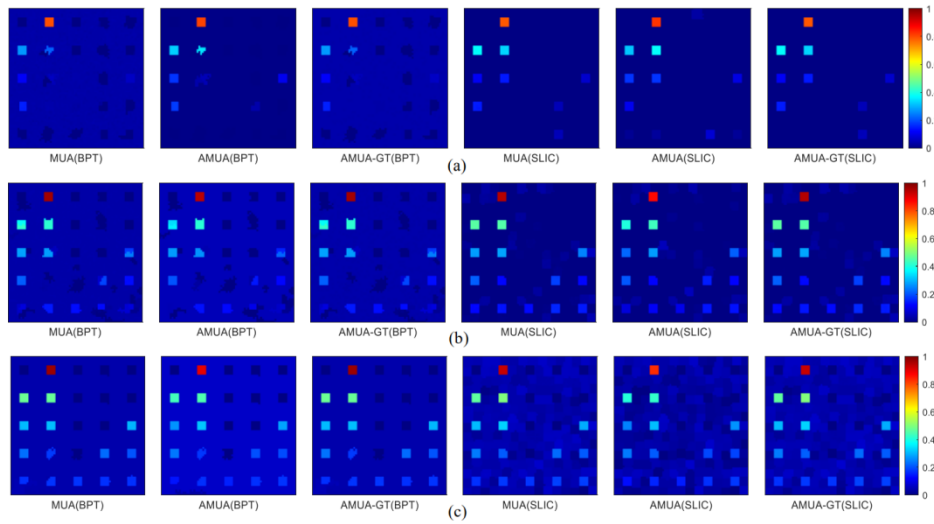

Fig. 12. The first comparison of abundance images estimated by different algorithms
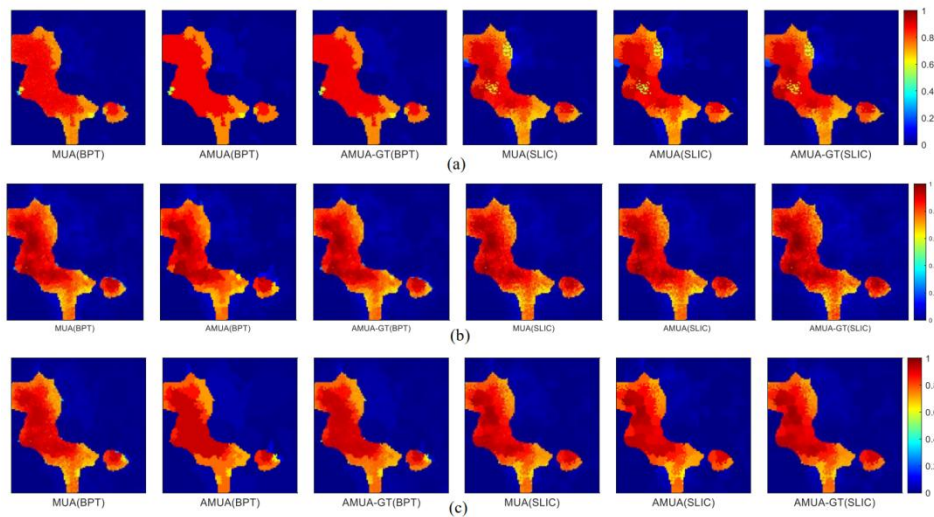

Fig. 13. The second comparison of abundance images estimated by different algorithms

Table 5. The comparison of SRE values by different algorithms.

Algorithms / Data	DC1 data cube			DC2 data cube		
	20 dB	**30 dB**	**40 dB**	**20 dB**	**30 dB**	**40 dB**
MUA(BPT)	13.393	18.257	21.8	13.928	16.963	18.54
AMUA-GT(BPT)	13.435	18.281	21.959	13.788	16.134	18.68
AMUA(BPT)	12.715	18.217	21.806	13.554	14.9704	16.32
MUA(SLIC)	11.346	15.731	22.126	14.757	18.328	20.52
AMUA-GT(SLIC)	11.380	15.770	22.302	14.774	18.184	22.07
AMUA(SLIC)	10.530	13.832	20.17	14.488	17.60	20.38

6.   Conclusion

The efficient AMUA algorithm is proposed in this paper for unmixing hyperspectral images, which can be applied to national land resources detection. The AMUA model is constructed by applying the MAP to the MUA model. The relationships among regularisation parameters, estimated abundances and estimated noise variances are explored and applied to ADDM to update the regularisation parameters automatically during the optimization process.

Two simulated hyperspectral datasets and one real HRSI were employed to verify the effectiveness and accuracy of the proposed algorithm. All the observations prove that the calculation efficiency is markedly improved without manual parameter selection at the cost of negligible accuracy. A series of sensitivity experiments were also undertaken to demonstrate the robustness of the AMUA algorithm.

The limitation lies in the fact that the noise in the observed HRSI is assumed as independent and identically Gaussian distribution, which is not suitable for many practical situations. Therefore, the sparse unmixing for HRSI contaminated with non-Gaussian noise will be studied in the future.

References

1. Zhang T., Hou M., Zhou T., Liu Z., Cheng W., and Cheng Y.,"Land-use classification via ensemble dropout information discriminative extreme learning machine based on deep convolution feature,"Computer Science and Information Systems., vol. 17, no.2, pp.427-443,2020.
2. Liu H., Li C., and Xu L.,"Dimension Reduction and Classification of Hyperspectral Images based on Neural Network Sensitivity Analysis and Multi-instance Learning,"Computer Science and Information Systems . , vol. 16, no.2, pp.443-468,2019.
3. Cheng, R., Yu, W., Song, Y., Chen, D., Ma, X. and Cheng, Y. Intelligent Safe Driving Methods Based on Hybrid Automata and Ensemble CART Algorithms for Multihigh-Speed Trains[J]. IEEE Transactions on Cybernetics,vol. 49, no.10, pp. 3816-3826,2019.
4. Liu, G., Chen, X., Zhou, R., Xu, S., Chen, Y.C. and Chen, G. Social learning discrete Particle Swarm Optimization based two-stage X-routing for IC design under Intelligent Edge Computing architecture[J]. Applied Soft Computing. 10, 10721,2021
5. Liu, G., Zhang, X., Guo, W., Huang, X., Liu, W., Chao, K. and Wang, T. Timing-Aware Layer Assignment for Advanced Process Technologies Considering Via Pillars. IEEE

Transactions on Computer-Aided Design of Integrated Circuits and Systems, vol. 41, no.6, pp. 1957-1970,2022.

6. Cheng, H., Wu, L., Li, R., Huang, F., Tu, C. and Yu, Z. Data recovery in wireless sensor networks based on attribute correlation and extremely randomized trees [J]. Journal of Ambient Intelligence and Humanized Computing, vol. 12, no.1, pp245-259,2021.

7. Liu, G., Zhu, Y., Xu, S., Chen, Y.C. and Tang H. PSO-Based Power-Driven X-Routing Algorithm in Semiconductor Design for Predictive Intelligence of IoT Applications. Applied Soft Computing, 114: 108-114,2022.

8. Li F. "Low-Rank and Spectral-Spatial Sparse Unmixing for Hyperspectral Remote Sensing Imagery," Wireless Communications and Mobile Computing., vol. 2021, no.1, pp.1-14, 2021.

9. Yu, Z., Zheng, X., Huang, F., Guo, W., Sun, L. and Yu, Z. A framework based on sparse representation model for time series prediction in smart city[J]. Frontiers of Computer Science, 15(1): 1-13,2021.

10. Lu, Z., Liu, G. and Wang, S. Sparse neighbor constrained co-clustering via category consistency learning [J]. Knowledge-Based Systems, 201, 105987,2020.

11. Shen, S., Yang, Y. and Liu, X. Toward data privacy preservation with ciphertext update and key rotation for IoT [J]. Concurrency and Computation: Practice and Experience, e6729. https://doi.org/10.1002/cpe.6729,2021.

12. Wang, Le et al., "A survey of methods incorporating spatial information in image classification and spectral unmixing," International Journal of Remote Sensing., vol. 37, no.16, pp.3870-3910, 2016.

13. Feng, Ruyi et al., "Rolling guidance based scale-aware spatial sparse unmixing for hyperspectral remote sensing imagery," Remote Sensing., vol.9, no. 12 , pp.1218-1221, 2017.

14. Shi, Zhenwei et al., "Collaborative Sparse Hyperspectral Unmixing Using $ l_{0} $ Norm," IEEE Transactions on Geoscience and Remote Sensing., vol. 56, no. 9, pp.5495-5508, 2018.

15. Ertürk, Alp, Marian-Daniel Iordache, and Antonio Plaza, "Sparse unmixing-based change detection for multitemporal hyperspectral images," IEEE Journal of Selected Topics in Applied Earth Observations and Remote Sensing., vol. 9, no.2, pp.708-719, 2015

16. Qi, Lin et al., "Region-Based Multiview Sparse Hyperspectral Unmixing Incorporating Spectral Library," IEEE Geoscience and Remote Sensing Letters., vol. 7, no.16, pp.1140-1144, 2019.

17. Palsson, Burkni et al., "Hyperspectral unmixing using a neural network autoencoder," IEEE Access., vol.6, pp.25646-25656, 2018.

18. Dai, Y., Wang, S., Chen, X., Xu, C. and Guo, W..Generative adversarial networks based on Wasserstein distance for knowledge graph embeddings[J]. Knowledge-Based Systems, 190: 105165,2020.

19. Li, X. Y., Lin, W., Liu, X., Lin, C., Pai, K. and Chang, J. Completely Independent Spanning Trees on BCCC Data Center Networks with an Application to Fault-Tolerant Routing[J]. IEEE TRANSACTIONS ON PARALLEL AND DISTRIBUTED SYSTEMS, vol.33, no.8 pp. 1939-1952,2022.

20. Iordache, Marian-Daniel, José M. Bioucas-Dias, and Antonio Plaza, "Sparse unmixing of hyperspectral data," IEEE Transactions on Geoscience and Remote Sensing., vol.49, no.6, pp.2014-2039,2011.

21. Iordache, Marian-Daniel, José M. Bioucas-Dias, and Antonio Plaza."Total variation spatial regularization for sparse hyperspectral unmixing," IEEE Transactions on Geoscience and Remote Sensing., vol. 50, no.11, pp.4484-4502, 2012.

22. Zhang, Shaoquan et al. "Spectral–spatial weighted sparse regression for hyperspectral image unmixing," IEEE Transactions on Geoscience and Remote Sensing., vol.56, no.6, pp.3265-3276,2018.

23. Borsoi, Ricardo Augusto et al. "A Fast Multiscale Spatial Regularization for Sparse Hyperspectral Unmixing," IEEE Geoscience and Remote Sensing Letters., vol.4, no.16, pp.598-602,2018.

24. Cheng, Y., Jiang, H., Wang, F., Hua, Y., Feng, D., Guo, W. and Wu, Y. Using High-Bandwidth Networks Efficiently for Fast Graph Computation [J]. IEEE Transactions on Parallel and Distributed Systems, vol.30, no.5, pp. 1170-1183,2019.

25. Wang, S., Wang, Z., Lim, K. L., Xiao, G. and Guo, W. Seeded random walk for multi-view semi-supervised classification [J]. Knowledge-Based Systems, 222:107016, 2021.

26. Zhang, H., Li, J. L., Liu, X. M. and Chen, D. Multi-dimensional feature fusion and stacking ensemble mechanism for network intrusion detection [J]. Future Generation Computer Systems, 122: 130-143,2021.

27. Zhang, Y., Lu, Z. and Wang, S. Unsupervised feature selection via transformed auto-encoder[J]. Knowledge-Based Systems, 215: 106748,2021 .

28. Fu, Y. G., Ye, J. F., Yin, Z. F., Chen, L., Wang, Y. and Liu, G. Construction of EBRB classifier for imbalanced data based on Fuzzy C-Means clustering[J]. Knowledge-Based Systems, 234: 107590,2021.

29. Arridge, Simon et al. "Solving inverse problems using data-driven models," Acta Numerica., vol. 28, pp. 1-174, 2019.

30. Ren, Dongwei et al. "Simultaneous Fidelity and Regularization Learning for Image Restoration"., arXiv preprint arXiv:1804.04522 , 2018.

31. Cao, Chunhong et al. "Hyperspectral Image Denoising via Subspace-Based Nonlocal Low-Rank and Sparse Factorization," IEEE Journal of Selected Topics in Applied Earth Observations and Remote Sensing., vol.3, no.12, pp. 973-988,2019.

32. Fu, Y. G., Zhuang, J. H., Chen, Y. P., Guo, L. and Wang, Y. A framework for optimizing extended belief rule base systems with improved Ball trees [J]. Knowledge-Based Systems, 210: 106484,2020.

33. Liu, G., Chen, Z., Zhuang, Z., Guo, W. and Chen, G. A unified algorithm based on HTS and self-adapting PSO for the construction of octagonal and rectilinear SMT[J]. Soft Computing, vol.24, no.6, pp.3943-3961,2020.

34. Liu, N., Pan, J. Sun, C., Ch, Su. An efficient surrogate-assisted quasi-affine transformation evolutionary algorithm for expensive optimization problems [J]. Knowledge-Based Systems, 209: 106418,2020.

35. Huang, Zhen et al. "Maximum a posteriori adaptation of network parameters in deep models," Conference of the International Speech Communication Association, ISCA, September 6-10, 2015, Dresden, Germany, pp. 1076-1080,2015.

36. Pereyra, M. . "Revisiting Maximum-A-Posteriori Estimation in Log-Concave Models." SIAM Journal on Imaging Sciences., vol. 12, no.1, pp.650-670,2019.

37. Feng, Ruyi, Yanfei Zhong, and Liangpei Zhang. "Adaptive spatial regularization sparse unmixing strategy based on joint MAP for hyperspectral remote sensing imagery," IEEE Journal of Selected Topics in Applied Earth Observations and Remote Sensing., vol.9, no.12, pp. 5791-5805,2016.

38. Chen, N. N., Gong, X. T., Wang, Y. M., Zhang, C. Y. and Fu, Y. G. Random clustering forest for extended belief rule-based system [J]. Soft Computing, vol.25, no.6, pp.4609-4619,2021.

39. Fu, Y. G., Huang, H. Y., Guan. Y., Wang, Y., Liu, W. and Fang, W. EBRB cascade classifier for imbalanced data via rule weight updating [J]. Knowledge-Based Systems, 223: 107010,2021..

40. Guo, L., Li, M. and Xu, D. Efficient Approximation Algorithms for Maximum Coverage with Group Budget Constraints [J]. Theoretical Computer Science, 788:53-65,2019.

41. Li H. , Lin Z. . "Accelerated Alternating Direction Method of Multipliers: an Optimal O(1/K) Nonergodic Analysis", Journal of Scientific Computing, vol.79, no.2, pp. 671-699,2019.

42. Babacan, S. Derin, Rafael Molina, and Aggelos K. Katsaggelos. "Bayesian compressive sensing using Laplace priors," IEEE Transactions on image processing., vol.19, no.1, pp.53-63,2009.
43. Bioucas-Dias J M, Nascimento J M P. "Hyperspectral subspace identification," IEEE Transactions on Geoscience and Remote Sensing. vol. 46, no.8, pp.2435-2445,2008.
44. Miguel A et al. "Hyperspectral image segmentation using a new spectral unmixing-based binary partition tree representation," IEEE Transactions on Image Processing., vol. 23, no.8, pp.3574-3589,2014.
45. R. Achanta, A. Shaji, K. Smith, A. Lucchi, P. Fua, and S. Süsstrunk, "SLIC superpixels compared to state-of-the-art superpixel methods," IEEE transactions on pattern analysis and machine intelligence. vol. 34, no.11, pp.2274–2282,2012.

Yalan Li received the B.S. degree from Hunan University of Science and Technology, Xiangtan, China in 2004 and received the M.S., and Ph.D. degrees in communication engineering from Huazhong Normal University, Wuhan, China, in 2007, and 2017, respectively. He is currently an Associate Professor with the School of Physics and Electronic Electrical Engineering, XiangNan University, Chenzhou, China. His research interests include image processing and pattern recognition, etc.

Qian Du received the B.S. degree from Qufu Normal University, Qufu, China in 2004 and received the B.S., M.S. degrees in communication engineering from Huazhong Normal University, Wuhan, China, in 2004. She is currently an Associate Professor with the School of Information Science and Engineering, Linyi University, Linyi, China. Her research interests include wireless networks algorithm and Internet of Things, etc.

Yixuan Li received the B.S. degree in Nankai University Binhai College, Tianjin, China, in 2019. He is currently pursuing the master's degree with the School of Information Science and Engineering, Hunan Institute of Science and Technology, Yueyang, China. His research interests include UAV-aided communications, intelligent reflecting surface and wireless power communication networks.

Wenwu Xie received the B.S., M.S., and Ph.D. degrees in communication engineering from Huazhong Normal University, Wuhan, China, in 2004, 2007, and 2017, respectively. He is currently an Associate Professor with the School of Information Science and Engineering, Hunan Institute of Science and Technology, Yueyang, China. His research interests include communication algorithm, such as channel estimation, equalizer, encoding/decoding, etc.

Jing Yuan received the Ph.D. degree in Information and Communication Engineering in 2019 from Tsinghua University, Beijing, China. She is currently an Associate Professor in the Institute of Disaster Prevention. Her current research interests include Machine Learning, Hyperspectral Image Unmixing and Sparse Representation.

Shang Lin Li received his doctor degree in Computer Science and Technology from Computer and Information Department of Hefei University of Technology in 2017. He is currently an associate professor of Computer Application Technology in the

Computer Science and Artificial Intelligence department at Xiangnan University. His research interests include Computer Graphic, Rapid Modeling and Machine Learning.

Qi Chen received the B.S. degree in control technology and instruments from China Jiliang University, Hangzhou,China,in 2002 and received the M.S. and Ph.D. degrees in communication engineering from Huazhong Normal University, Wuhan, China, in 2006, and 2019, respectively. She is also an Associate Professor at the College of Computer and Information Engineering of Hubei Normal University, Huangshi, China.Her research interets include image processing and computer vision.